Received: 15 May 2023 | Revised: 13 July 2023 | Accepted: 13 July 2023

DOI: 10.1111/jace.19375

Journal of the American Ceramic Society

SPECIAL ISSUE ARTICLE

Phase stability and cation partitioning in compositionally complex rare earth aluminates and aluminate-zirconate mixtures

Yueh-Cheng Yu[1] | **William O. Nachlas**[2] | **David L. Poerschke**[1]

[1]Department of Chemical Engineering and Materials Science, University of Minnesota, Twin Cities, Minneapolis, Minnesota, USA

[2]Department of Geoscience, University of Wisconsin-Madison, Madison, Wisconsin, USA

Correspondence
David Poerschke, Department of Chemical Engineering and Materials Science, University of Minnesota, Twin Cities, Minneapolis, MN.
Email: dpoersch@umn.edu

Submitted to the Journal of the American Ceramic Society special issue "2nd Century Trailblazers"

Funding information
Division of Materials Research, Grant/Award Number: DMR-2011401; NASA, Grant/Award Number: 80NSSC21C0071; Division of Electrical, Communications and Cyber Systems, Grant/Award Number: ECCS-2025124

Abstract

Multicomponent oxides have received significant recent attention due to their potential for improved property tunability. In simple structures, compositionally complex oxides can be stabilized by increased configurational entropy and are sometimes called "high entropy" ceramics. In phases with multiple cation sublattices or complex stoichiometries, it is more difficult to achieve high configurational entropy. However, there is limited knowledge about the factors influencing stability and solubility limits in many systems. This study investigated the limits on the stability of rare earth (RE) aluminates containing mixtures of RE cations including Gd, La, Nd, Yb, and Y in cases where (i) a fixed RE:Al ratio attempts to constrain the material into a single-phase aluminate or (ii) a two-phase aluminate, and in equilibrium with RE zirconates that readily dissolve multiple RE^{3+}. The results show that it is difficult to form single-phase, equimolar mixed-RE aluminates encompassing a range of RE^{3+} sizes. Instead, the RE^{3+} selectively partition into specific phases based on RE-size trends in the constituent binary systems. The results are discussed in terms of the phase stability and cation partition trends and potential applications.

KEYWORDS
aluminates, phase equilibria, phase separation, rare earths, zirconate

1 | INTRODUCTION

The past decade has brought burgeoning interest in the discovery, synthesis, and characterization of compositionally complex oxides offering improved properties for a variety of functional and structural applications. The current excitement about these ceramics, which feature multiple cations mixed on individual crystal sublattices, grew from the results of Rost et al.[1] showing that multication rock salt solid solutions were stabilized by high configurational entropy. Similar approaches have been applied to a variety of oxide ceramic structures and composition ranges.[2–7] In some cases, the designs seek to use configurational entropy to stabilize crystal structures that are unstable in lower-order systems containing subsets of the same components. In other cases, compositions are designed to tune the

properties between end members or by leveraging the role of disorder governing thermal or mass transport properties without a particular focus on entropy.

There is an ongoing discussion about the role of entropy in stabilizing these multicomponent materials, the best metrics to quantify and compare configurational entropy (S_{config}), and the appropriate naming conventions.[4,8,9] This debate stems in part from the varying degrees to which chemical disorder can be achieved in diverse oxide crystal structures. In one limit are structures such as rock salt (MO, where M is a metal) and fluorite (MO_2) that have a single cation sublattice that can flexibly accommodate a variety of cation substitutions. The ideal S_{config} for a multisublattice structure (e.g., one for cations and one for anions) can be calculated according to Eq. 1 for the fraction f_i of component i distributed randomly on the a^x sites of sublattice x, and the gas constant R.[10]

$$S_{\text{config}}^{\text{ideal}} = \frac{-R\sum_{x=1}^{x} a^x \sum_{i=1}^{N} f_i^x \ln\left(f_i^x\right)}{\sum_{x=1}^{x} a^x}. \quad (1)$$

Considering a notional compositionally complex oxide comprising a random, equiatomic mixture of five metal cations in MO or MO_2, the ideal S_{config} are 0.8R and 0.54R per mole of atoms, respectively. Due to the absence of disorder on the oxygen sublattice, these values are less than an equivalent five-component metal alloy ($S_{\text{config}} = 1.61\text{R}$) and do not meet the classic definition of "high entropy" ($S_{\text{config}} \geq 1.61\text{R}$), but still exhibit entropic stabilization in some systems.[2,3,9,11,12]

In another limit are oxides with multiple distinct cation sublattices that, due to cation size or charge constraints, limit mixing between sublattices. One commonly studied system is the perovskite family defined as ABO_3, where the A and B cations are coordinated by 12 and 6 oxygen, respectively.[11] Random mixing of five cations on either A or B yields $S_{\text{config}} = 0.32\text{R}$. In another example, mixing five cations on a single sublattice in the garnet system ($A_3B_2T_3O_{12}$, where the A, B, and T cation sites are coordinated by 8, 6, and 4 oxygen, respectively) yields S_{config} in the range 0.16R to 0.24R depending on the sublattice with the mixed cations. Families of compositionally complex compounds in these structures, as well as other aluminates, silicates, and zirconates, have also been synthesized and characterized.[6,12–18] While meeting a definition of compositional complexity, these examples do not have particularly "high entropy," and thus have less capacity for reducing the free energy by increasing configurational entropy in the case of unfavorable enthalpy of mixing for the components.

Despite the reduced role of entropy, interesting questions emerge about the thermodynamic stability of compositionally complex, multisublattice oxides. These questions, elaborated below, deal with the relative importance of average versus individual ionic radii in determining stability and constraints imposed by the requirements to fill multiple sublattices with appropriately sized cations. The rare earth (RE) aluminates, which form multiple crystal structures in the binary RE_2O_3-Al_2O_3 systems and have varying degrees of accessible configurational entropy, provide a useful model system to explore these questions. The relevant binary compounds are defined in the next paragraph before the discussion of their compositionally complex variants.

Figure 1 shows the general trends for the stability of the four possible aluminate line compounds as a function of the Shannon-Prewitt radii[32,33] for the RE^{3+} with a coordination number (CN) of 8. $RE_4Al_2O_9$, which forms for the smaller and mid-sized RE, exhibits a monoclinic structure at room temperature (and thus is typically abbreviated "M") and transforms to an orthorhombic polymorph at high temperature.[34,35] $REAlO_3$ forms with perovskite-type structures (P) for virtually all RE radii; distortions for the cations smaller than Nd^{3+} lead to an orthorhombic structure (*o*-perovskite, oP) while the larger RE form a rhombohedral (trigonal) structure denoted *r*-perovskite or rP.[36,37] The $RE_3Al_5O_{12}$ stoichiometry crystallizes in the garnet (G) structure with Al filling the B and T sites. This phase is stable for the smaller RE^{3+} and is also known for persistent metastability for other stoichiometries.[38–40] Finally, $REAl_{11}O_{18}$ is an alkali-earth deficient magnetoplumbite (β-Al_2O_3) variant formed for the largest RE.[41,42] Available experimental and calculated thermodynamic data[37,43] suggest that perovskite and monoclinic aluminate stability increases and decreases, respectively, with increasing RE size. G has the strongest size dependence on Gibbs energy with the most negative formation enthalpy for RE^{3+} radii near Y.

The stoichiometry and the nature of the cation sublattices influence the achievable configurational entropy in compositionally complex aluminates formed by mixing different RE^{3+} with a fixed Al stoichiometry (Table 1). This variation, combined with the size-dependent trends in stability (Figure 1) and the need for specific RE:Al stoichiometry to form each phase, prompts the following questions related to the ability to form compositionally complex aluminate solid solutions:

1. To what degree is the capability to form a compositionally complex, single-phase solid solution determined by the range of cation sizes versus the average cation size?
2. Does fixing the availability of cations for one sublattice (e.g., Al in aluminates) to match the stoichiometry of a particular phase increase the likelihood of forming a version of that phase with a compositionally

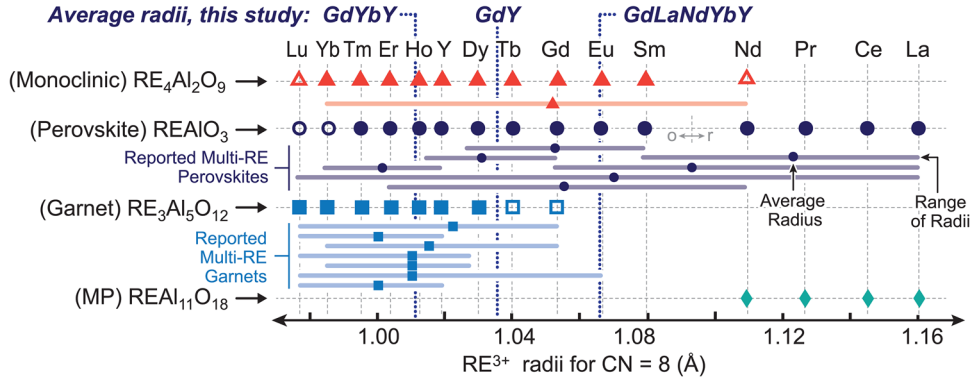

FIGURE 1 Stability ranges for RE aluminates, adapted from Ref. (19). The larger filled symbols indicate the single-RE aluminates considered to be stable and open symbols indicate cases where conflicting reports suggest the phase has limited stability or is metastable. The average (small symbols) and range (shaded bars) of RE^{3+} sizes for reported single phase, multi-RE monoclinic,[20] perovskite,[21–24] and garnet[25–31] aluminates are shown for comparison.

TABLE 1 Definition and characteristics of phases observed in this study.

Name	Formula	Abbreviation	Space group	S^{ideal}_{config}/R*
Bixbyite (REO)	$(RE,Zr)O_{1.5+\delta}$	R, REO	$Ia\bar{3}$	**
Fluorite	$(Zr,RE)O_{2-\delta}$	F	$Fm\bar{3}m$	**
Monoclinic	$RE_4Al_2O_9$	M	$P2_1/c$	0.43
o-Perovskite	$REAlO_3$	oP	Pnma	0.32
r-Perovskite	$REAlO_3$	rP	$R\bar{3}c$	0.32
Garnet	$RE_3Al_5O_{12}$	G	$Ia\bar{3}d$	0.24
Magnetoplumbite	$REAl_{11}O_{18}$	MP	$P6_3/mmc$	0.05

*Calculated per mole of atoms assuming random mixing of 5 RE elements on the site(s) containing RE.
**S_{config} depends on the Zr concentration and oxygen stoichiometry and falls in the range ~0.6R to ~0.85R.

complex second sublattice containing cations that do not independently stabilize that phase? Furthermore, would the ability to form that phase change if it were in a multiphase field without the sublattice stoichiometry constraint? For instance, would defining a material with a 5:3 RE:Al ratio ($RE_3Al_5O_{12}$, matching the garnet stoichiometry) and containing Yb^{3+} and Y^{3+}, which do form garnet, and Gd^{3+}, Nd^{3+}, and La^{3+}, which do not readily form garnet, favor forming a single-phase garnet solid solution? If so, would increasing the RE:Al ratio to fall between $REAlO_3$ and $RE_3Al_5O_{12}$, and thus presumably form a two-phase mixture that distributes the large RE^{3+} in perovskite and the small RE^{3+} in garnet, reduce the incorporation of the large RE^{3+} in the garnet?

3. Does introducing a phase capable of dissolving a large range of cations, thus serving as a "sink" for cations rejected from other phases, change the tendency to form multicomponent solid solutions?

The behaviors are ultimately determined by composition-dependent changes in the lattice stability of each phase. Absent a complete thermodynamic assessment of the relevant systems, initial insight is gained by analyzing literature reports on the formation of single-phase RE aluminates containing multiple RE elements. These data, collected in Figure 1, show that all reported multi-RE garnets[25–31] have average RE radii located near the center of the garnet stability range. Additionally, except for select cases where a single RE^{3+} (either Gd^{3+} or Eu^{3+}) from outside the stability range is included, all the elements included in these multi-RE garnets form garnet independently. Conversely, the reports of multi-RE perovskites[21–24] cover the entire range of RE sizes, including one example where the single phase covers the entire range from Lu to La, albeit as a thin film.[22] Likewise, the single report of a multi-RE monoclinic phase[20] includes a wide range of cation sizes within the monoclinic stability range. One conclusion is that the aluminates only incorporate RE^{3+} into a solid solution if the RE will independently form a given phase. However, most reports focus on examples where single phases are formed, and there is presently limited knowledge about the extent and limits of solid solution formation.

TABLE 2 Compositions of mixed aluminate materials studied (Gd:La:Nd:Yb:Y = 1:1:1:1:1, mean RE^{3+} radius = 1.065 Å).

Formula	Simple stoichiometry	Al/RE (atom ratio)	Full cation stoichiometry
$RE_4Al_2O_9$	$Al_{33}RE_{67}$	0.5	$Al_{33}Gd_{13}La_{13}Nd_{13}Yb_{13}Y_{13}$
	$Al_{40}RE_{60}$	0.67	$Al_{40}Gd_{12}La_{12}Nd_{12}Yb_{12}Y_{12}$
$REAlO_3$	$Al_{50}RE_{50}$	1	$Al_{50}Gd_{10}La_{10}Nd_{10}Yb_{10}Y_{10}$
	$Al_{55}RE_{45}$	1.25	$Al_{55}Gd_9La_9Nd_9Yb_9Y_9$
$RE_3Al_5O_{12}$	$Al_{63}RE_{37}$	1.67	$Al_{63}Gd_8La_8Nd_8Yb_8Y_8$

More information about the stability of these compositionally complex phases is gained by coupling studies about the existence of single-phase material with analysis of cation partitioning (preferential enrichment or exclusion) in multiphase mixtures. Seeking to answer the questions posed above, this experimental study examines the RE^{3+} partitioning in mixtures of RE aluminates and mixtures of RE aluminates in equilibrium with RE oxide and the RE zirconate fluorite phase. In addition to providing insights about the stability limits for compositionally complex materials, the results for these systems have practical importance for the design of multiphase aluminate-zirconate materials of interest as prospective thermal and environmental barrier coatings (T/EBC) in turbine engines.[38,44,45]

2 | EXPERIMENTAL METHODS

2.1 | Material selection

Two material families were studied. The first are aluminate compositions corresponding to the stoichiometric M, P, and G compounds along with compositions in the two-phase fields between them (Table 2). The mixed aluminate samples were formulated with an equimolar mixture of Gd, La, Nd, Yb, and Y that samples most of the entire RE^{3+} size range with an average radius near the center of the range. Based on the data in Figure 1, if the stability is determined by the average RE radius, single-phase monoclinic and *o*-perovskite could form, but single-phase garnet would only be expected if the modest configurational entropy is sufficient to overcome the instability of garnet containing the larger RE^{3+}.

The second family is a series of mixed aluminate-zirconate compositions with three overall Al:RE:Zr ratios and three different RE mixtures (Table 3 and Figure 2). One pair of Al:RE:Zr ratios varies the $AlO_{1.5}$ content at fixed RE:Zr ratio ($Al_{10}RE_{76}Zr_{14}$* and $Al_{30}RE_{60}Zr_{10}$). A second pair varies the RE:Zr ratio at fixed $AlO_{1.5}$ content ($Al_{30}RE_{60}Zr_{10}$ and $Al_{30}RE_{35}Zr_{35}$). The primary motivation to select these stoichiometries is to strategically sample two- and three-phase fields in the ternary $AlO_{1.5}$-$REO_{1.5}$-ZrO_2 systems including combinations of the G, P, and M in equilibrium with fluorite or the ZrO_2-saturated RE oxide. An additional consideration is that the selected stoichiometries avoid the ordered pyrochlore (Py) and δ-phase zirconates in favor of fluorite in most of the ternary subsystems, facilitating analysis of the partitioning behavior in the case where the zirconate phase tends to form a disordered solid solution. Finally, these aluminate-zirconate mixtures with RE:Zr ≥ 1 are more likely to have desirable characteristics for T/EBC applications, and facilitate comparison with results from prior studies related to that application.[38,46,47] In addition to the equimolar Gd, La, Nd, Yb, and Y (RE = GdLaNdYbY henceforth), mixed aluminate-zirconate compositions were formulated with equimolar mixtures of Gd and Y (RE = GdY) and Gd, Yb, and Y (RE = GdYbY). These combinations have average radii near the center of the garnet and monoclinic ranges, respectively, shown in Figure 1, and were selected to probe cation partitioning in these phases that are less stable in the RE = GdLaNdYbY mixture.

2.2 | Material synthesis and equilibration

Well-mixed oxide powders were prepared by co-precipitation using the previously reported method.[38] Solutions were prepared from nitrates of Al, Gd, La, Nd, Yb, and Y (99.9% pure, Alfa Aesar) in ethanol and Zr oxy-nitrate (99.9%, Alfa Aesar) in water. The calibrated solutions were mixed to yield the desired cation stoichiometries and added dropwise to excess aqueous ammonium hydroxide. The hydroxide precipitates were washed in ethanol, dried, pyrolyzed to 1000°C, and then either ground with an alumina mortar and pestle or ball milled using zirconia media. The powders were cold pressed into 6 mm diameter pellets, placed onto Pt foil in covered alumina crucibles, and annealed for 250 and 500 h

* Subscript in abbreviated composition notation represents the mol% of the corresponding oxide on a single cation basis, rounded to the closest integer value.

TABLE 3 Compositions of mixed aluminate-zirconate materials studied.

Simple stoichiometry	RE/Zr ratio	$AlO_{1.5}$ (mol %)	Gd:La:Nd:Yb:Y (atom ratio)	Mean RE^{3+} radius (Å)	Full cation stoichiometry
$Al_{30}RE_{35}Zr_{35}$	1	30	1:0:0:0:1	1.036	$Al_{30}Gd_{18}Y_{18}Zr_{35}$
			1:0:0:1:1	1.009	$Al_{30}Gd_{12}Yb_{12}Y_{12}Zr_{35}$
			1:1:1:1:1	1.065	$Al_{30}Gd_{7}La_{7}Nd_{7}Y_{7}Yb_{7}Zr_{35}$
$Al_{30}RE_{60}Zr_{10}$	5.7	30	1:0:0:0:1	1.036	$Al_{30}Gd_{30}Y_{30}Zr_{10}$
			1:0:0:1:1	1.009	$Al_{30}Gd_{20}Yb_{20}Y_{20}Zr_{10}$
			1:1:1:1:1	1.065	$Al_{30}Gd_{12}La_{12}Nd_{12}Yb_{12}Y_{12}Zr_{10}$
$Al_{10}RE_{76}Zr_{14}$	5.7	10	1:0:0:0:1	1.036	$Al_{10}Gd_{38}Y_{38}Zr_{14}$
			1:0:0:1:1	1.009	$Al_{10}Gd_{25}Yb_{25}Y_{25}Zr_{14}$
			1:1:1:1:1	1.065	$Al_{10}Gd_{15}La_{15}Nd_{15}Yb_{15}Y_{15}Zr_{14}$

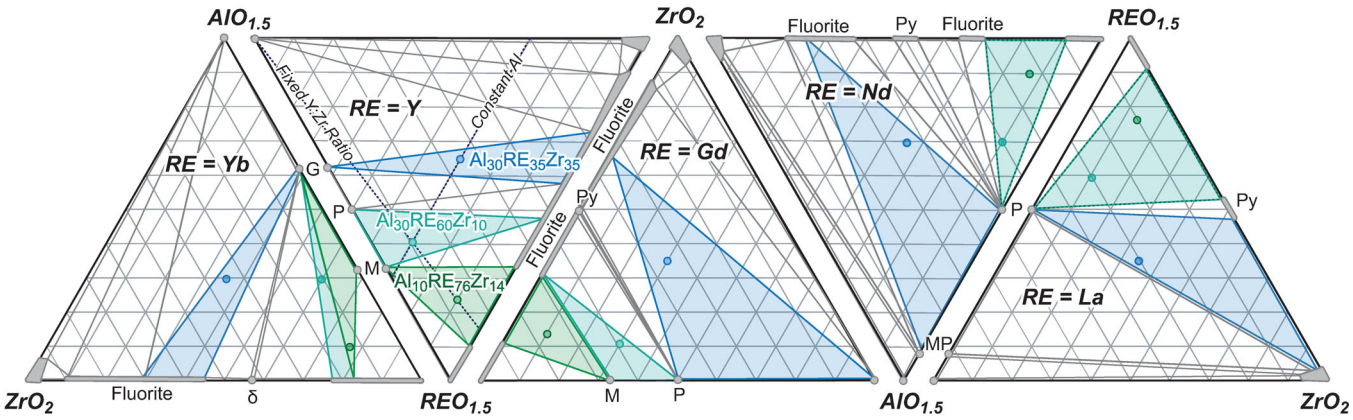

FIGURE 2 Ternary $AlO_{1.5}$-$REO_{1.5}$-ZrO_2 isothermal sections representing the expected equilibria at 1500°C with increasing RE^{3+} size from left to right; adapted from literature reports.[38,48–50] For Yb, Y, and Gd, the REO is the cubic (bixbyite) structure and for Nd and La it is the A-type (P32/m).

at 1500°C in lab air. No changes in phase constitution were observed between 250 and 500 h. The reported composition data are from the samples equilibrated for 500 h.

2.3 | Characterization

A portion of each equilibrated pellet was ground to a powder for X-ray diffraction (XRD, Rigaku Miniflex 600, step = 0.04°, dwell time per step = 3.6 s). The other portion was mounted in epoxy and polished to a 1 μm finish for electron probe microanalysis (EPMA) and to use backscattered scanning electron microscopy (BS-SEM, Hitachi SU8230) to characterize the microstructures.

The EPMA characterization of the RE = GdY and GdYbY samples used previously reported methods.[39,46] EPMA of samples with RE = GdLaNdYbY used a Cameca SX100/SXFive FE-EPMA with beam energy of 12 keV and current of 30 nA. Measurements were performed with a low overvoltage condition to reduce absorption path length and minimize activation volume for measuring submicron grains. The analyzing crystals were LIF for Yb L_α, LLIF for La L_β, Nd L_β, and Gd L_β, PET for Y L_α, Zr L_α, and LTAP for Al K_α. The on-peak and off-peak counting times were 20/10 s for Zr, Y, Nd, and Gd and 50/25 s for La, Yb, and Al. Interference corrections were applied to Al for interference by Yb, to Y for interference by La, and to Gd for interference by Nd. The standards were $GdPO_4$ (NMNH 168488), $LaPO_4$ (NMNH 168490), $NdPO_4$ (NMNH 168492), $YbPO_4$ (NMNH 168498), YPO_4 (NMNH 168499), synthetic Al_2O_3, and synthetic zircon (ORNL #257). The oxygen concentration was determined by stoichiometry. Depending on the grain size and distribution, point measurements were made for between four and ten grains of each phase. Average compositions are reported; standard deviations were generally less than 0.3 mol% for each oxide but occasionally as high as 1 mol%, especially for smaller grains.

TABLE 4 Observed phases after 500 h at 1500°C, labeled according to the abbreviations in Table 1.

Mixed aluminate-zirconate materials					
RE constitution		$Al_{30}RE_{35}Zr_{35}$	$Al_{30}RE_{60}Zr_{10}$		$Al_{10}RE_{76}Zr_{14}$
GdY		F + G	F + M + oP		F + M + R
GdYbY		F + G	F + oP + M + R		M + oP + R
GdLaNdYbY		MP + F + G + rP	F + rP + R		F + rP + R
Mixed aluminate materials					
RE constitution	$Al_{33}RE_{67}$	$Al_{40}RE_{60}$	$Al_{50}RE_{50}$	$Al_{55}RE_{45}$	$Al_{63}RE_{37}$
GdLaNdYbY	rP + R (+ M)	M + rP + R	oP + rP (+ M)	G + rP	MP + G + rP

Note: Parentheses indicate a small phase fraction.

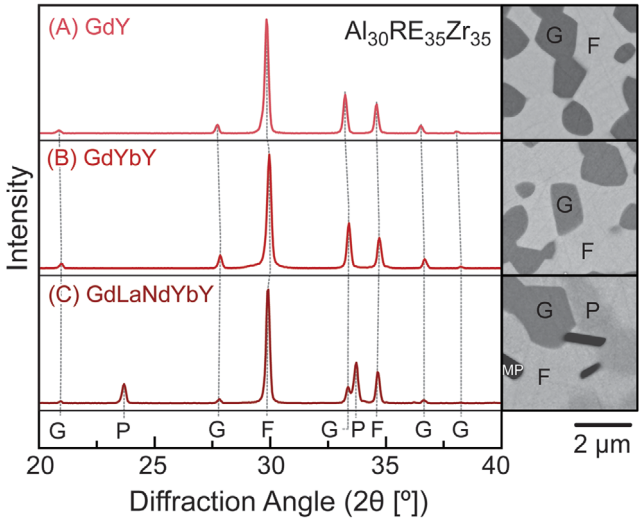

FIGURE 3 XRD patterns and representative BS-SEM micrographs from the $Al_{30}RE_{35}Zr_{35}$ mixed aluminate-zirconate samples equilibrated at 1500°C. Reflections labeled "P" refer to rP polymorphs.

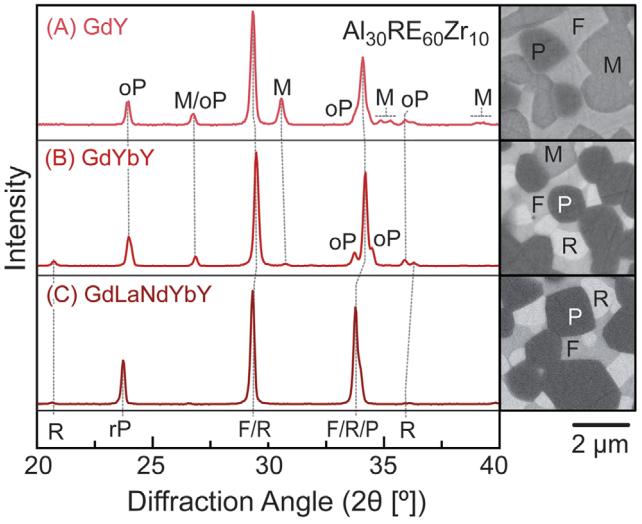

FIGURE 4 XRD patterns and representative BS-SEM micrographs from the $Al_{30}RE_{60}Zr_{10}$ mixed aluminate-zirconate samples equilibrated at 1500°C. Reflections labeled "P" are characteristic of both the oP and rP polymorphs.

3 | RESULTS AND DISCUSSION

The combination of XRD, microstructure, and EPMA composition data (e.g., the RE:Al ratio for the aluminates) described below was used to identify the phases present in each sample (Table 4). This section first describes the general trends in the equilibrium phase assemblages, followed by discussion of the cation partitioning in each sample and phase.

3.1 | Equilibrium phases

3.1.1 | Aluminate-zirconate mixtures

XRD and microstructure data for the $Al_{30}RE_{35}Zr_{35}$ samples are shown in Figure 3. Garnet and fluorite coexist in equilibrium for RE = GdY and GdYbY, while the GdLaNdYbY sample contains magnetoplumbite and the *r*-perovskite in addition to garnet and fluorite. This means that the presence of Yb^{3+} and Y^{3+} is sufficient to stabilize Gd in the garnet phase expected for the smaller RE elements (Figure 1), while the larger range of RE radii in the GdLaNdYbY sample is better accommodated by a mixture of the garnet, *r*-perovskite, and magnetoplumbite aluminates.

Figure 4 shows XRD and microstructure observations for the $Al_{30}RE_{60}Zr_{10}$ samples. The RE = GdY composition formed a mixture of monoclinic, fluorite, and *o*-perovskite. This assemblage is consistent with the expected single-RE ternary assemblages for both Gd^{3+} and Y^{3+} shown in Figure 2. Adding Yb^{3+} (RE = GdYbY) stabilizes REO in addition to fluorite and the monoclinic and *o*-perovskite aluminates. The addition of the larger RE^{3+} in the GdLaNdYbY sample destabilizes the monoclinic aluminate in favor of the *r*-perovskite, which coexists with REO and fluorite. All the $Al_{10}RE_{76}Zr_{14}$ compositions form REO as one of the equilibrium phases (Figure 5). The sample

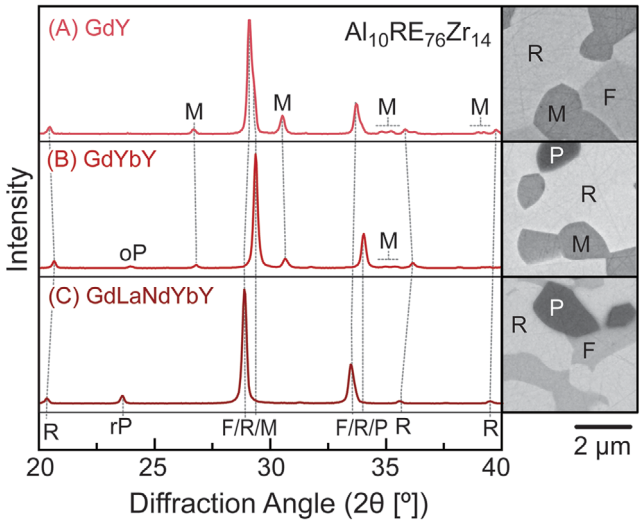

FIGURE 5 XRD patterns and representative BS-SEM micrographs from the $Al_{10}RE_{76}Zr_{14}$ mixed aluminate-zirconate samples equilibrated at 1500°C. Reflections labeled "P" are characteristic of both the oP and rP polymorphs.

RE = GdY forms fluorite and the monoclinic aluminate with the REO. Adding Yb destabilizes the fluorite in favor of the *o*-perovskite, while the addition of Nd^{3+} and La^{3+} in the RE = GdLaNdYbY sample destabilizes the monoclinic aluminate, the perovskite structure shifts to *r*-perovskite, and fluorite reappears as an equilibrium phase. The observation that increasing the number of RE^{3+} in the material either maintains or increases the number of equilibrium phases runs counter to the expectation that increased configurational entropy by adding more RE would drive the system toward a smaller number of solution phases.

3.1.2 | Aluminates

XRD patterns and representative microstructures for the Zr-free, mixed aluminate samples are shown in Figure 6. The *r*-perovskite phase appeared in every sample, regardless of the Al:RE ratio. The identity of the additional equilibrium phases varies with the Al:RE ratio. The $Al_{33}RE_{67}$ sample, which corresponds to the stoichiometry of the monoclinic aluminate ($RE_4Al_2O_9$), forms a mixture of primarily *r*-perovskite and REO. Occasional grains of the monoclinic phase were observed in the microstructure but the fraction was too small to be evident by XRD. The implication is that there is sufficient driving force to form the perovskite ($REAlO_3$) with the larger RE^{3+}, so most of the available Al is consumed to form perovskite. As a result, the monoclinic aluminate is destabilized, and the remaining smaller RE^{3+} forms the REO. Increasing the alumina content in the sample to $Al_{40}RE_{60}$ increases the fraction of

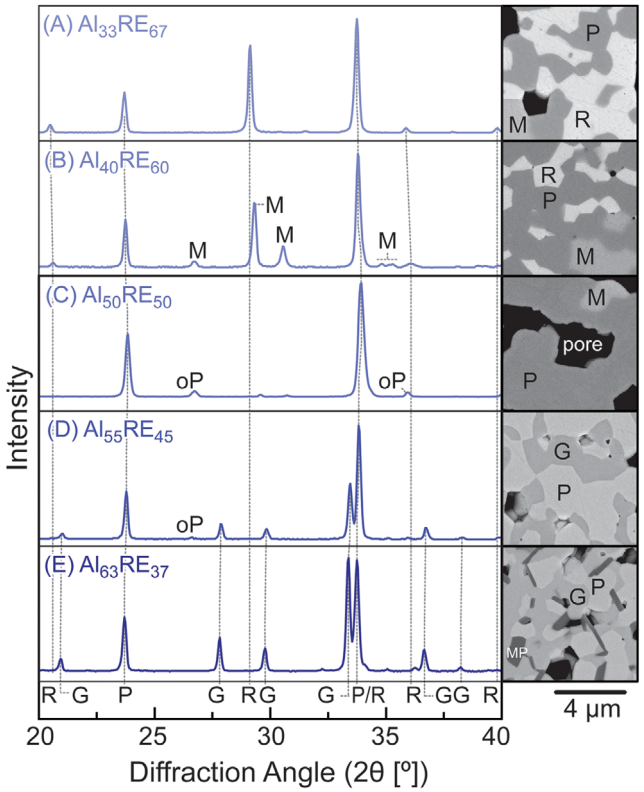

FIGURE 6 XRD patterns and BSE-SEM micrographs from the mixed aluminate samples with RE = GdLaNdYbY equilibrated at 1500°C. Reflections labeled "P" are characteristic of both the oP and rP polymorphs.

the M phase, but the *r*-perovskite and REO remain in significant fractions. This observation means that M is only stabilized once enough Al is present to satisfy the $REAlO_3$ formation by the larger RE^{3+}.

The further increase in the alumina content from $Al_{40}RE_{60}$ to $Al_{50}RE_{50}$ (corresponding to the perovskite stoichiometry $REAlO_3$) produces a mixture of perovskite with a small fraction of the monoclinic likely due to the synthesized composition being slightly Al-deficient. The XRD pattern for this sample shows characteristic peaks for the oP polymorph in addition to rP, and, as elaborated in the discussion of the cation partitioning below, the EPMA data also suggest that two perovskite variants are present in this sample. Garnet appears upon increasing the Al fraction to $Al_{55}RE_{45}$. The *o*-perovskite was not evident in the microstructures or found by distinguishing composition in the EPMA data, but oP characteristic reflections with very low intensity in the XRD data suggest there may be a small fraction. The apparent replacement of oP by the garnet aluminate suggests that garnet is the preferred phase for the smaller RE^{3+} if there is sufficient Al^{3+} to consume the RE while forming garnet. Finally, the equilibrium assemblage for $Al_{63}RE_{37}$, which corresponds to the

TABLE 5 Phase compositions in the mixed aluminate-zirconate samples with RE = GdY measured by EPMA (mol%).

Phase	Sample	$AlO_{1.5}$	$GdO_{1.5}$	$YO_{1.5}$	ZrO_2
Monoclinic	$Al_{30}RE_{60}Zr_{10}$	33.8	34.8	31.4	0.0
	$Al_{10}RE_{76}Zr_{14}$	33.4	30.6	36.0	0.0
o-Perovskite	$Al_{30}RE_{60}Zr_{10}$	50.5	28.4	21.1	0.0
Garnet	$Al_{30}RE_{35}Zr_{35}$	62.3	16.9	20.7	0.1
REO	$Al_{10}RE_{76}Zr_{14}$	0.0	39.8	44.5	15.7
Fluorite	$Al_{30}RE_{35}Zr_{35}$	0.7	18.0	15.7	65.6
	$Al_{30}RE_{60}Zr_{10}$	0.7	28.9	36.8	33.7
	$Al_{10}RE_{76}Zr_{14}$	0.6	35.0	33.3	31.1

garnet stoichiometry $RE_3Al_5O_{12}$, contains *r*-perovskite and magnetoplumbite in addition to garnet.

3.2 | Phase compositions and RE cation partitioning behavior

This section describes the tendency for each RE^{3+} to preferentially partition into or out of each phase. The analysis was performed by calculating the normalized RE^{3+} fractions in each phase from the compositions measured by EPMA. These fractions were then compared to the bulk average RE fractions of 0.5, 0.33, and 0.2 for the equimolar RE combinations in RE = GdY, GdYbY, and GdLaNdYbY, respectively. The uncertainty in these fractions was calculated by propagating the typical standard deviations in the measured compositions into the calculation of the reported RE^{3+} fractions.

3.2.1 | Aluminate-zirconate mixtures

The phase compositions for the GdY aluminate-zirconate samples are listed in Table 5. The aluminate stoichiometries match the expected total Al:RE ratios and contain essentially no ZrO_2. The REO contains no $AlO_{1.5}$ but dissolved approximately 16 mol% ZrO_2, which is slightly greater than the solubility limits shown in the ternary sections in Figure 2. The fluorite has limited (<1 mol %) $AlO_{1.5}$ solubility and varies in RE:Zr ratio since each sample falls in a different phase field.

The normalized RE composition for each phase is plotted along the Gd-Y composition axis at the base of the Gibbs triangles in Figure 7, and for each RE in each phase in Figure 8A–C. The garnet in $Al_{30}RE_{35}Zr_{35}$ is enriched in Y^{3+}, while Gd^{3+} partitions into the fluorite. This behavior is consistent with the fact that garnet is more stable for the smaller RE^{3+}. However, the magnitude of these shifts is modest, suggesting that although Gd^{3+} garnet does not exist at equilibrium at this temperature, there is also not a strong driving force for it to partition out of the Y-stabilized garnet. The shifts away from the equimolar RE fraction are more pronounced in the $Al_{30}RE_{60}Zr_{10}$ sample, with the perovskite enriched in Gd^{3+} while excess Y^{3+} partitions into the monoclinic and fluorite. For $Al_{10}RE_{76}Zr_{14}$, the fluorite and monoclinic are slightly enriched in Gd^{3+} and the REO is enriched in Y^{3+}, but the magnitude of the shifts in $Al_{10}RE_{76}Zr_{14}$ is smaller than in the other two samples. Notably, the direction of the composition shifts for fluorite and monoclinic are reversed between $Al_{30}RE_{35}Zr_{35}$ and $Al_{30}RE_{60}Zr_{10}$ and $Al_{30}RE_{60}Zr_{10}$ and $Al_{10}RE_{76}Zr_{14}$, respectively. This suggests that the garnet, perovskite, and REO phases exhibit stronger driving force for partitioning, while the fluorite and monoclinic respond by incorporating the cations that are preferentially rejected from those phases.

Table 6 lists the measured phase compositions in the RE = GdYbY samples, and the RE composition shifts are plotted in Figures 7 and 8D–F. The addition of Yb^{3+} reduces the tendency for Y^{3+} to selectively partition between phases while the general trends for Gd^{3+} are the same as the RE = GdY samples. For $Al_{30}RE_{35}Zr_{35}$, the fluorite is again enriched in Gd^{3+}, while the garnet is equally enriched in Y^{3+} and Yb^{3+}. For $Al_{30}RE_{60}Zr_{10}$, the perovskite is enriched in Gd^{3+} while the fluorite and REO become enriched in Yb^{3+}. The only noticeable shift in the Y^{3+} concentration from the bulk average is the monoclinic phase in $Al_{30}RE_{60}Zr_{10}$. $Al_{10}RE_{76}Zr_{14}$ shows strong enrichment in Gd^{3+} and depletion in Yb^{3+} in perovskite, and modest Gd^{3+} enrichment in monoclinic.[†] The shifts in $Al_{30}RE_{60}Zr_{10}$ and $Al_{10}RE_{76}Zr_{14}$ occur along a line of approximately constant Y concentration except a slight Y^{3+} enrichment in the monoclinic phase and reduction of Y^{3+} in perovskite.

The measured compositions for the RE = GdLaNdYbY phases (Table 7) were used to calculate the RE^{3+} partition-

[†] In Figure 7(C), the nominal bulk composition for the $Al_{10}RE_{76}Zr_{14}$ sample sits slightly outside the triangle formed by the three phases; this small deviation is ascribed to uncertainty in the as-synthesized or measured compositions.

TABLE 6 Phase compositions in the mixed aluminate-zirconate samples with RE = GdYbY measured by EPMA (mol%).

Phase	Sample	$AlO_{1.5}$	$GdO_{1.5}$	$YbO_{1.5}$	$YO_{1.5}$	ZrO_2
Monoclinic	$Al_{30}RE_{60}Zr_{10}$	32.8	21.1	21.2	24.9	0.0
	$Al_{10}RE_{76}Zr_{14}$	34.1	25.8	16.3	23.8	0.1
Perovskite	$Al_{30}RE_{60}Zr_{10}$	50.1	20.2	12.3	17.3	0.0
	$Al_{10}RE_{76}Zr_{14}$	50.2	25.9	8.6	15.3	0.0
Garnet	$Al_{30}RE_{35}Zr_{35}$	61.9	11.1	12.8	13.6	0.5
REO	$Al_{30}RE_{60}Zr_{10}$	1.0	17.3	34.5	27.6	19.6
	$Al_{10}RE_{76}Zr_{14}$	0.3	23.7	29.0	29.2	17.9
Fluorite	$Al_{30}RE_{35}Zr_{35}$	0.9	12.3	10.5	10.7	65.7
	$Al_{30}RE_{60}Zr_{10}$	1.2	17.4	25.5	23.0	32.9

TABLE 7 Phase compositions in the mixed aluminate-zirconate samples with RE = GdLaNdYbY measured by EPMA (mol%).

Phase	Sample	$AlO_{1.5}$	$GdO_{1.5}$	$LaO_{1.5}$	$NdO_{1.5}$	$YbO_{1.5}$	$YO_{1.5}$	ZrO_2
r-Perovskite	$Al_{30}RE_{35}Zr_{35}$	49.6	8.5	20.5	17.3	1.3	2.6	0.1
	$Al_{30}RE_{60}Zr_{10}$	49.3	10.5	17.7	16.0	2.1	4.3	0.0
	$Al_{10}RE_{76}Zr_{14}$	49.2	3.7	31.4	14.0	0.7	0.8	0.0
Garnet	$Al_{30}RE_{35}Zr_{35}$	62.4	7.5	0.4	1.9	14.4	13.2	0.2
REO	$Al_{30}RE_{60}Zr_{10}$	0.1	14.4	2.1	5.3	35.0	27.5	15.6
	$Al_{10}RE_{76}Zr_{14}$	0.0	21.0	8.7	15.7	23.2	22.8	8.6
Fluorite	$Al_{30}RE_{35}Zr_{35}$	0.0	7.5	1.4	3.9	9.9	9.0	68.3
	$Al_{30}RE_{60}Zr_{10}$	0.6	14.1	4.5	7.9	22.7	21.0	29.3
	$Al_{10}RE_{76}Zr_{14}$	0.0	15.1	15.1	16.5	13.6	13.7	26.0

ing trends plotted in Figure 8G–I. For all three samples, the most significant trend is the tendency for the perovskite to contain essentially no Yb^{3+}, only small amounts of Y^{3+}, and to be significantly enriched in Nd^{3+} and La^{3+} relative to the equimolar bulk average. The other phases become correspondingly enriched in the Yb^{3+} and Y^{3+}, and the shifts in the Gd^{3+} concentration are comparatively modest.

For $Al_{30}RE_{35}Zr_{35}$, the relative magnitudes of these shifts are greater for the garnet compared to the fluorite. The plate-like morphology and small size of the magnetoplumbite grains made it difficult to avoid secondary fluorescence from adjacent phases during quantitative composition analysis, but it appears to conform to the $REAl_{11}O_{18}$ stoichiometry with La^{3+} as the primary RE component. The relative cation partitioning behavior for the REO and fluorite in $Al_{30}RE_{60}Zr_{10}$ is similar to the garnet and fluorite in $Al_{30}RE_{35}Zr_{35}$. The $Al_{10}RE_{76}Zr_{14}$ sample forms the same phases as $Al_{30}RE_{60}Zr_{10}$, but its partitioning behavior is different. Specifically, the perovskite shows a more significant enrichment in La^{3+}, which makes up almost two thirds of the RE^{3+} in the aluminate, while the REO shows only slight enrichment in Yb^{3+} and Y^{3+}, and the RE^{3+} constitution in the fluorite matches the equimolar average within the experimental uncertainty.

The differences between $Al_{30}RE_{60}Zr_{10}$ and $Al_{10}RE_{76}Zr_{14}$ can be rationalized based on the strong driving force for La to enter the perovskite and the lower Al^{3+} content to stabilize the perovskite aluminate in the latter. In $Al_{30}RE_{60}Zr_{10}$, all the La^{3+} (12 mol% of the total cations) is consumed to form perovskite well before the Al^{3+}, which makes up 30 mol % of the cations. Thus, most of the Nd^{3+} and approximately a third of the Gd^{3+} also contribute to perovskite formation before the Al^{3+} is consumed. Conversely, there is more La^{3+} than Al^{3+} in $Al_{10}RE_{76}Zr_{14}$ so there are still Nd^{3+} and La^{3+} remaining to enter the fluorite once the Al^{3+} is consumed to form perovskite.

3.2.2 | Mixed aluminates

The measured compositions of the phases formed in the mixed aluminate samples (Table 8) were used for the analysis of the RE^{3+} partitioning behavior shown in Figure 9. For all cases except $Al_{50}RE_{50}$, the perovskite compositions follow the same trend as in the mixed aluminate-zirconate samples, with little Yb^{3+}, slightly more Y^{3+}, and significant enrichment in Nd^{3+} and La^{3+}, while the Gd^{3+} concentration remains near the bulk equimolar fraction. The excess Yb^{3+} and Y^{3+} partitions primarily into the REO for

TABLE 8 Phase compositions in mixed aluminate samples measured by EPMA (mol%).

Phase	Sample	$AlO_{1.5}$	$GdO_{1.5}$	$LaO_{1.5}$	$NdO_{1.5}$	$YbO_{1.5}$	$YO_{1.5}$
Monoclinic	$Al_{33}RE_{67}$	31.7	17.6	8.3	11.8	12.5	18.1
	$Al_{40}RE_{60}$	33.2	14.0	5.7	8.2	19.0	20.0
	$Al_{50}RE_{50}$	33.1	8.7	3.9	5.1	30.5	18.7
r-Perovskite	$Al_{33}RE_{67}$	49.5	9.9	19.1	16.8	1.4	3.3
	$Al_{40}RE_{60}$	49.5	10.8	16.4	15.4	2.6	5.2
	$Al_{50}RE_{50}$	50.1	10.2	11.6	11.7	7.6	8.8
	$Al_{55}RE_{45}$	49.9	11.0	15.3	14.6	3.4	5.8
	$Al_{63}RE_{37}$	49.6	9.4	18.8	18.2	1.3	2.7
o-Perovskite	$Al_{50}RE_{50}$	49.9	10.1	9.5	8.6	11.5	10.4
Garnet	$Al_{55}RE_{45}$	61.8	6.3	0.8	1.8	16.4	12.9
	$Al_{63}RE_{37}$	62.3	8.2	0.5	2.2	14.1	12.7
REO	$Al_{33}RE_{67}$	0.1	20.4	2.0	6.7	37.4	33.4
	$Al_{40}RE_{60}$	0.3	13.9	1.5	4.2	48.1	31.9

$Al_{33}RE_{67}$ and $Al_{40}RE_{60}$, and in the garnet in $Al_{55}RE_{45}$ and $Al_{63}RE_{37}$. The monoclinic aluminate shows a slight enrichment in the Yb^{3+} and Y^{3+} and depletion in Nd^{3+} and La^{3+} relative to the bulk, but the tendency for partitioning is weaker than the other phases.

The preferential partitioning in the perovskite phase is less evident in the $Al_{50}RE_{50}$ sample (Figure 9C). The EPMA revealed two populations of perovskite grains: one type has slightly elevated Nd^{3+} and La^{3+} concentrations while the other type is slightly enriched in Yb^{3+} and Y^{3+}. Additionally, the XRD pattern for this sample showed characteristic peaks for *o*-perovskite polymorph in addition to the *r*-perovskite. Based on these data and the trends in the binary aluminates, it is assumed that the *r*-perovskite is enriched in Nd^{3+} and La^{3+} and the *o*-perovskite is slightly enriched in Yb^{3+} and Y^{3+}. Notably, the trend for partitioning in *o*-perovskite is reversed from the observations with RE = GdY and GdYbY, likely because those samples contained other phases that readily accommodated the smaller RE^{3+}. The small fraction of monoclinic grains present in the sample are enriched in Yb^{3+} and Y^{3+} and contain little Gd^{3+}, Nd^{3+}, and La^{3+}.

3.2.3 | RE cation partitioning trends

To compare the behavior of each phase across all samples, the results of the partitioning analysis for the RE = GdLaNdYbY samples were grouped by phase and replotted in Figure 10. The results show that except for *r*-perovskite, all phases show a relative enrichment in Yb^{3+} and Y^{3+}, and depletion in Nd^{3+} and La^{3+}. The results for garnet are essentially equivalent for every sample in which it appears, regardless of the phase(s) it coexists with (Figure 10A). The behavior of the monoclinic aluminate is less consistent (Figure 10C). Yb^{3+} partitions strongly into the monoclinic phase in the case when it coexists as a minor fraction with perovskite ($Al_{50}RE_{50}$). However, when monoclinic also coexists with REO ($Al_{33}RE_{67}$ and $Al_{40}RE_{60}$), the Yb^{3+} partitions more strongly into the REO, resulting in proportionally higher concentrations of Y^{3+} and Gd^{3+} in the monoclinic.

The magnitude of the shifts for the fluorite and REO is smaller in the cases when they appear as the primary phases ($Al_{10}RE_{76}Zr_{14}$, open squares in Figure 10D and E) in equilibrium with a small fraction of aluminate (open squares in Figure 10B). The perovskite follows the opposite trend in most samples, with little Y^{3+} and Yb^{3+} and increased La^{3+} and Nd^{3+} content compared to the bulk average (Figure 10B). However, the perovskite deviates from this trend in cases where either a small fraction ($Al_{10}RE_{76}Zr_{14}$) leads to increased enrichment in La^{3+} or when perovskite is the predominate phase ($Al_{50}RE_{50}$) and more readily incorporates all RE^{3+}.

3.3 | Implications for phase stability in compositionally complex RE aluminates

Across the range of compositions studied, this investigation found no scenarios where RE^{3+} of varying size are uniformly incorporated into a single-RE aluminate in proportions matching the equimolar bulk fractions. Instead, the larger RE^{3+} (La^{3+} and Nd^{3+}) are the primary RE cations stabilizing the *r*-perovskite aluminate while the smaller Yb^{3+} and Y^{3+} are preferentially accommodated in the monoclinic and garnet aluminates, and the mixed REO. This tendency matches the stability trends in the single-RE aluminate systems (Figure 1) where perovskite is the most stable aluminate for large RE^{3+} and garnet

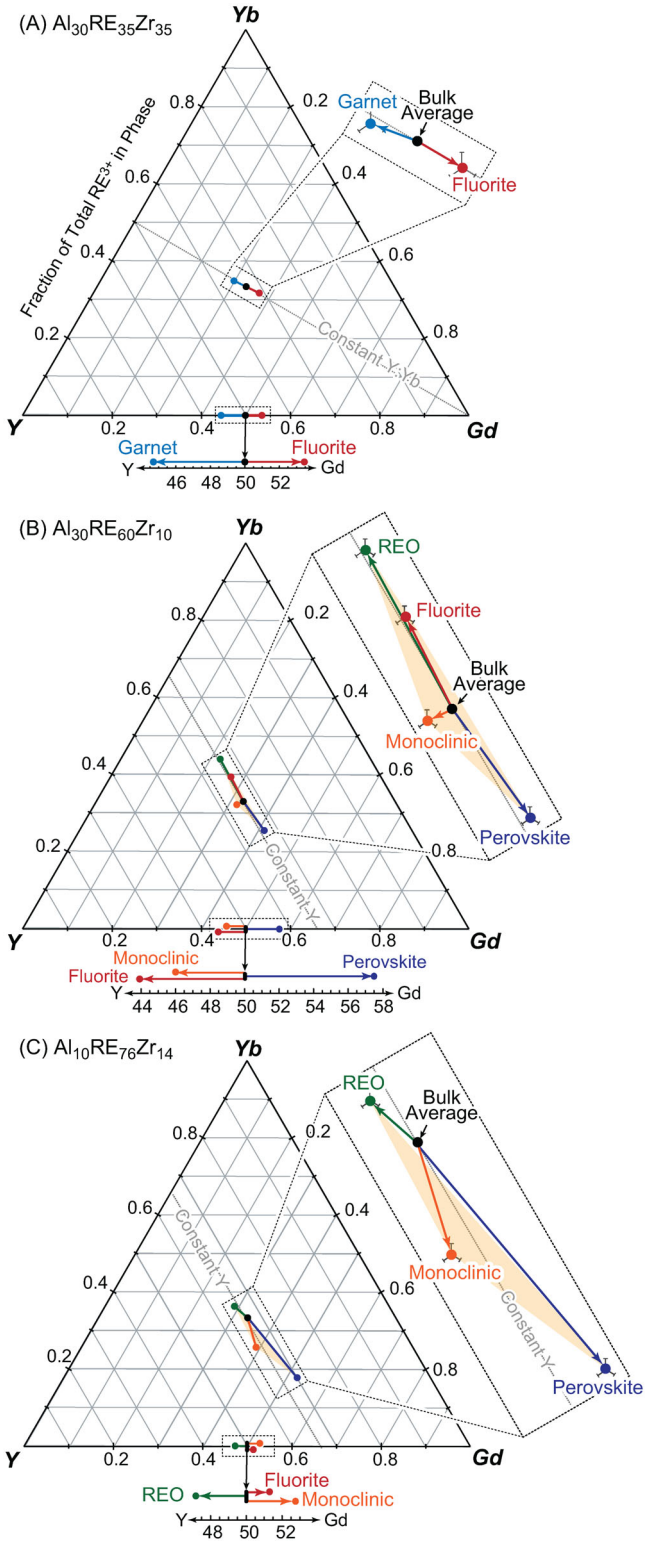

FIGURE 7 RE^{3+} constitution for the (A) $Al_{30}RE_{35}Zr_{35}$, (B) $Al_{30}RE_{60}Zr_{10}$, and (C) $Al_{10}RE_{76}Zr_{14}$ mixed aluminate-zirconate samples with either two or three RE types. Results for the binary RE = GdY are shown along the bottom axis and the ternary RE = GdYbY are shown in the center of each Gibbs triangle.

and monoclinic become more stable with decreasing RE cation size. One interpretation of these results is that the stabilizing effect of the increased S_{config} upon adding multiple RE^{3+} is insufficient to overcome the unfavorable enthalpies of formation and mixing for small RE^{3+} to dissolve into the *r*-perovskite, or for large RE^{3+} to dissolve into garnet and monoclinic. The cases that came closest to achieving equiatomic solid solution occurred in the perovskite polymorphs in the $Al_{50}RE_{50}$ sample, which has the highest possible S_{config} among the RE aluminate mixtures. For the RE aluminate-zirconate mixtures, the fluorite, which also has a comparatively high S_{config} and weaker cation site dependency for Zr^{4+} and RE^{3+}, shows less preferential RE^{3+} partitioning.

To further understand this behavior, we can compare the relative changes in the free energy to form each RE aluminate from the component oxides for the cases where the RE^{3+} are equally distributed between the phases and the cases with the experimentally measured RE^{3+} partitioning. Thermodynamic parameters for the RE aluminates from Wu and Pelton[43] were used for these illustrative calculations; the MP phase was not analyzed due to lack of data for all RE^{3+}. Figure 11A shows the Gibbs energy of formation (ΔG_f) at 1500°C for the La and Yb aluminates, representing the extremes in the behavior for the RE^{3+} studied, from pure oxide components. The convex hull (lowest free energy configuration) for Yb system includes monoclinic and garnet but falls just below the Yb-aluminate perovskite. As indicated by the black arrows, the free energies for the monoclinic and garnet aluminates become less negative as the RE^{3+} size increases toward La, while the free energy for perovskite becomes more negative. As a result, monoclinic and garnet fall above the hull for La. The values for the intermediate-sized RE^{3+} are not shown, but they fall along the arrows between the values for Yb and La.

The ΔG_f for the mixed-RE aluminates was then considered. To understand the degree to which S_{config} drives solid solution formation, notional values for ΔG_f were first calculated assuming ideal mixing *without* including the effect of S_{config}. Figure 11B shows the results for the case of an equimolar mixture of the five RE in each aluminate compared to that calculated based on the observed partitioning behavior of each aluminate. These calculations use the average of all observations for each phase, except that the results for the perovskite in $Al_{50}RE_{50}$ were excluded since there was limited partitioning in that case. The first key observation is that all three aluminates appear on the convex hull for both scenarios. The second key observation is that the curve based on the equilibrium, partitioned compositions falls below the curve for the equimolar RE^{3+} distribution. This result makes sense given that the higher Yb^{3+} and Y^{3+} concentrations in garnet and monoclinic,

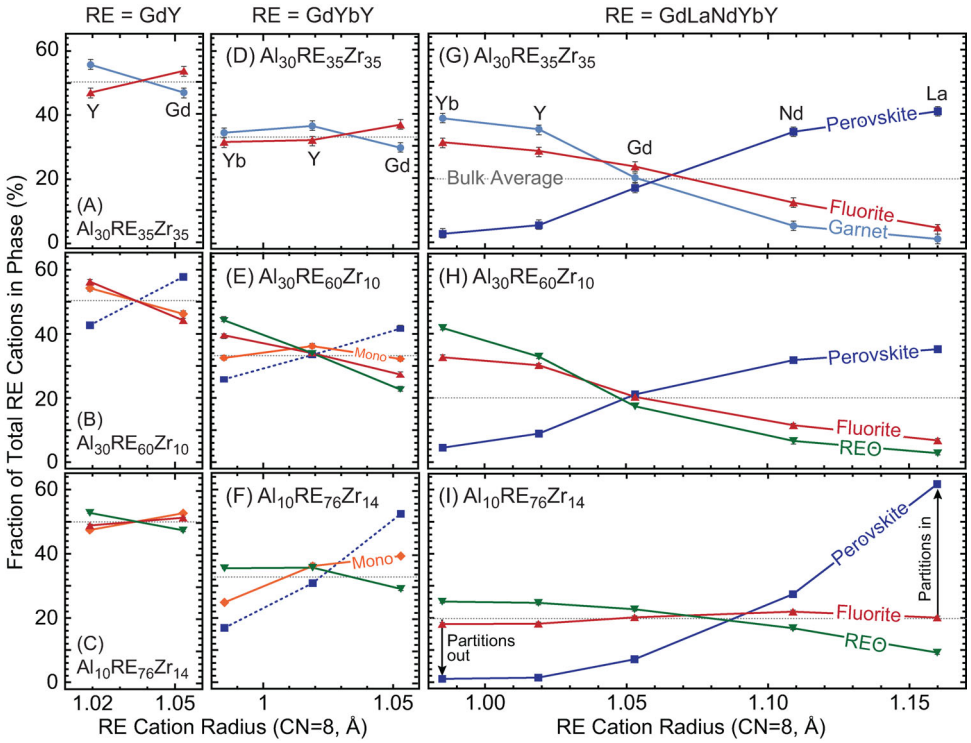

FIGURE 8 RE^{3+} partitioning in the mixed aluminate-zirconate samples with (A–C) RE = GdY, (D–F) RE = GdYbY, and (G–I) RE = GdLaNdYbY. Perovskite shown with dashed line is oP and the solid lines are rP. Some error bars are smaller than symbols.

and higher La^{3+} and Nd^{3+} fractions in perovskite, lower the free energy of each phase compared to the equimolar mixture.

Finally, the analysis considered the added effect of S_{config}, which was determined to be 0.19R, 0.28R, and 0.40R, respectively, for the experimentally observed garnet, perovskite, and monoclinic compositions. Notably, even though the equilibrium compositions exhibit significant RE^{3+} segregation between the phases compared to an equimolar RE^{3+} distribution, these S_{config} values are only slightly smaller than the values of 0.24R, 0.32R, and 0.43R for the equimolar RE mixing. In other words, the partitioning does not significantly decrease the configurational entropy compared to an ideal case with equimolar RE^{3+} distribution (i.e., no partitioning). Figure 11C shows ideal ΔG_f values including the effect of S_{config}. The reference state used for this analysis includes the S_{config} for the equimolar mixed $REO_{1.5}$. After including the S_{config}, the curves for the experimentally measured partitioned RE compositions and the equimolar RE scenarios are essentially coincident. This analysis shows that higher S_{config} in the equimolar RE mixture does lower the overall free energy more than the case where the RE cations partition between the phases. However, it also shows that the effect of the increased S_{config} is not enough to overcome the RE-size dependence on the formation enthalpies, which ultimately drives the cation partitioning.

It is not clear whether the similarity between the two curves in Figure 11C carries significance. One interpretation is that there is not a significant energetic benefit for the RE cations to partition in comparison to remaining uniformly distributed between the phases. However, this interpretation is at odds with the fact that RE partitioning is consistently observed across a variety of aluminate-containing stoichiometries. A more likely scenario is that there is an additional, nonideal contribution to the free energy due to mixing on the RE sublattice(s) in the aluminates that would increase the energetic benefit of the partitioning. However, a more rigorous computational thermodynamic assessment of these multicomponent systems is still necessary to enable further analysis of these effects.

With this context, the three questions posed in the introduction are revisited. The first question dealt with the relative importance of the individual versus average cation sizes in determining stability. The results show that having an average cation radius within the stability range for a specific phase is insufficient to stabilize that phase. This effect is most evident in the absence of the monoclinic phase in many of the samples with RE = GdLaNdYbY, even though the average radius for this RE mixture falls within the

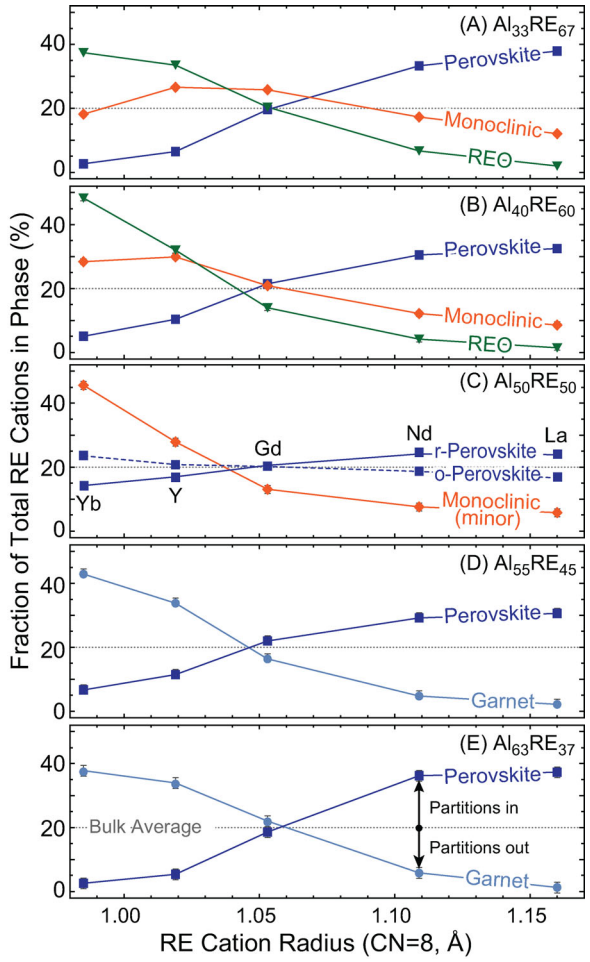

FIGURE 9 Normalized RE fractions for each phase in the mixed aluminate samples showing the cation partitioning trends. Except as noted in (C), perovskite is *r*-perovskite.

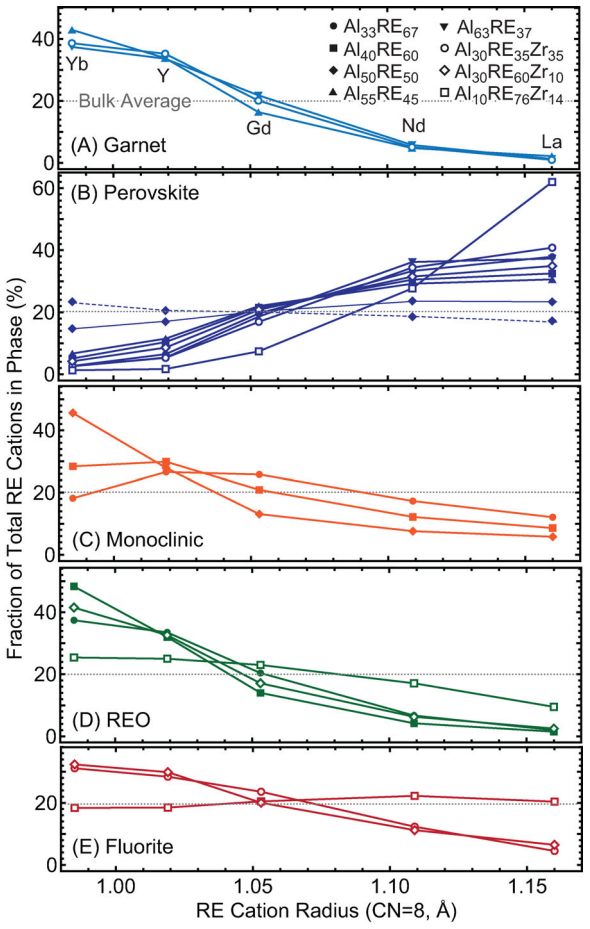

FIGURE 10 Trends in RE^{3+} partitioning in each phase across all samples with RE = GdLaNdYbY. In (B), the dashed line is oP and the solid lines are rP.

range for monoclinic stability. Instead, it appears energetically favorable to accommodate the combination of larger and smaller cations in a mixture of the perovskite and REO than the single monoclinic phase.

The second question sought to understand the influence of stoichiometric constraints imposed in a second sublattice on the stabilization of compositionally complex solid solutions. We found that controlling the RE:Al ratio was generally not effective in promoting the formation of a single-phase solid solution. This effect is most pronounced for the $Al_{33}RE_{67}$ and $Al_{63}RE_{37}$ samples, which correspond to the stoichiometries of the monoclinic ($RE_4Al_2O_9$) and garnet ($RE_3Al_5O_{12}$), respectively. The $Al_{33}RE_{67}$ sample formed essentially no monoclinic since the Al^{3+} instead stabilized the Nd- and La-rich perovskite, and monoclinic was only formed once additional Al^{3+} was added in the $Al_{40}RE_{60}$ sample. Likewise, the Nd^{3+} and La^{3+} in the $Al_{63}RE_{37}$ sample separated into the perovskite and magnetoplumbite rather than entering the garnet. Even $Al_{50}RE_{50}$ formed two perovskite polymorphs with equivalent Al:RE ratio, rather than a single phase.

The third question relates to the tendency for additional solid solution phases, in this case fluorite and the ZrO_2-saturated REO, to influence the formation of a multi-RE aluminate solid solution. Insight is gained by comparing the partitioning behavior for the Zr-free and Zr-containing samples shown with closed and open symbols, respectively, in Figure 10. For garnet, there is not a discernable difference between the two families of materials. Most of the perovskite compositions also follow similar trends regardless of whether they are in equilibrium with a zirconate or not. The perovskite in the $Al_{10}RE_{76}Zr_{14}$ sample is an exception, however, showing that the presence of large fractions of fluorite and ZrO_2-saturated REO that readily accommodate the smaller RE^{3+} allows the perovskite to become even more enriched in La^{3+} than when the perovskite exists in equilibrium with the other aluminates.

The results have implications for the future design of compositionally complex oxides. There are limits on the extent to which increased configurational entropy can be

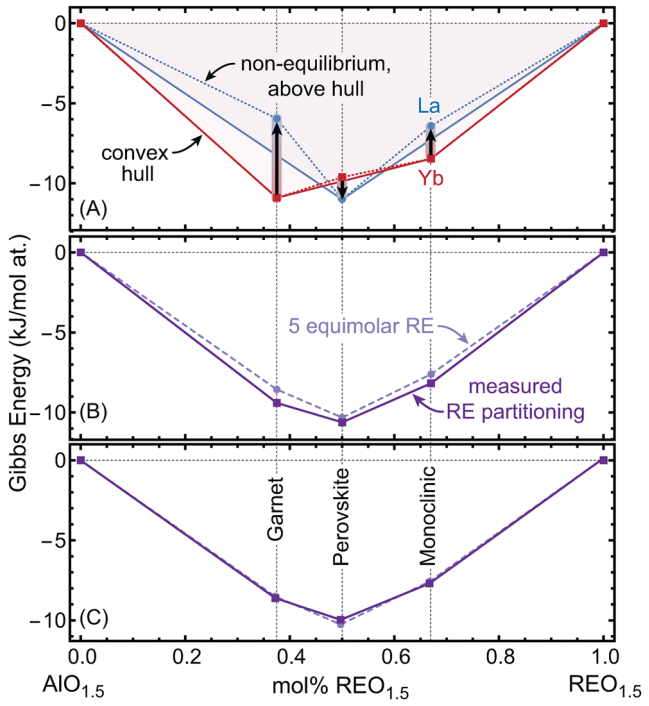

FIGURE 11 (A) Calculated ΔG_f at 1500°C for La- and Yb-garnet, perovskite, and monoclinic aluminates at 1500°C using thermodynamic parameters from Wu and Pelton.[43] In (A), the solid lines show the equilibrium convex hull, the dashed lines connect the energies above the hull, and the straight black arrows show the direction of change upon increasing the RE^{3+} size. (B) Calculated ΔG_f for mixed-RE aluminates with either equimolar mixing of the five RE in this study (dashed lines) and the average compositions of the measured equilibrium phases (solid line) assuming ideal mixing and without considering S_{config}. (C) Calculated ΔG_f for the cases in (B) but including the ideal S_{config}.

used to stabilize solid solutions based on structures with multiple sublattices. This conclusion was inferred from analysis of the range of the reported single-phase, multi-RE aluminates and confirmed by the experiments. Additionally, the results show that, with few exceptions, cations will partition between phases in mixed cation materials. This imposes additional constraints on the thermochemical compatibility of multicomponent oxides used in layered or composite systems.

4 | CONCLUSIONS

This study assessed the stability of rare earth aluminates and aluminate-zirconates containing equimolar mixtures of up to five RE^{3+} spanning the range of sizes. The analysis focused on changes in equilibrium phase assemblages and selective partitioning of the RE^{3+} between phases. The important conclusions are:

1. There were no scenarios in which all RE^{3+} dissolved into a single aluminate in equimolar proportions. Instead, the larger RE^{3+} (Nd^{3+} and La^{3+}) tended to stabilize and partition into the perovskite aluminate while the smaller RE^{3+} (Yb^{3+} and Y^{3+}) partitioned into the garnet and monoclinic aluminates.
2. Adding larger RE^{3+} in the mixture destabilized the monoclinic aluminate in favor of mixtures containing the larger RE^{3+} in the perovskite and the smaller RE^{3+} in the rare earth oxide and fluorite phases.
3. The addition of the RE zirconate fluorite did not significantly change the RE^{3+} partitioning trends in the aluminates except in cases where the aluminate was a minor phase.
4. The RE^{3+} closest to the average size for the mixture (Gd^{3+} for RE = GdLaNdYbY and Y^{3+} for the RE = GdYbY samples) was least likely to selectively partition between phases.

AUTHOR CONTRIBUTIONS

Y.-C.Y. and D.P. conceived the study. Y.-C.Y. prepared the samples, performed XRD and SEM characterization, and analyzed the data. Y.-C.Y. and W.N. performed EPMA. D.P. wrote the first manuscript draft, which all authors reviewed and edited.

ACKNOWLEDGMENTS

This research was partially supported by NASA award number 80NSSC21C0071 monitored by Dr. Cameron Bodenschatz, in collaboration with QuesTek Innovations LLC. Part of this work was carried out in the Characterization Facility at the University of Minnesota, which receives partial support from the NSF through the MRSEC (DMR-2011401) and the NNCI (ECCS-2025124) programs. The sponsors were not involved in the detailed study design, or the data collection, analysis, or interpretation. The authors are grateful to Josselyne Berrios for assistance with materials preparation and to Dr. Clémentine Hamelin for assistance with EPMA.

ORCID

David L. Poerschke https://orcid.org/0000-0002-6206-235X

REFERENCES

1. Rost CM, Sachet E, Borman T, Moballegh A, Dickey EC, Hou D, et al. Entropy-stabilized oxides. Nat Commun. 2015, 6. https://doi.org/10.1038/ncomms9485
2. Sarkar A, Djenadic R, Wang D, Hein C, Kautenburger R, Clemens O, et al. Rare earth and transition metal based entropy stabilised perovskite type oxides. J Eur Ceram Soc. 2018, 38(5):2318–27. https://doi.org/10.1016/j.jeurceramsoc.2017.12.058

3. Sarkar A, Wang QS, Schiele A, Chellali MR, Bhattacharya SS, Wang D, et al. High-entropy oxides: fundamental aspects and electrochemical properties. Adv Mater. 2019, 31(26). https://doi.org/10.1002/adma.201806236
4. McCormack SJ, Navrotsky A. Thermodynamics of high entropy oxides. Acta Mater. 2021, 202:1–21. https://doi.org/10.1016/j.actamat.2020.10.043
5. Hutterer P, Lepple M. Influence of composition on structural evolution of high-entropy zirconates-cationic radius ratio and atomic size difference. J Am Ceram Soc. 2023, 106(2):1547–60. https://doi.org/10.1111/jace.18832
6. Ridley MJ, Tomko KQ, Tomko JA, Hoglund ER, Howe JM, Hopkins PE, et al. Tailoring thermal and chemical properties of a multi-component environmental barrier coating candidate $(Sc_{0.2}Nd_{0.2}Er_{0.2}Yb_{0.2}Lu_{0.2})_2Si_2O_7$. Materialia. 2022, 26:101557. https://doi.org/10.1016/j.mtla.2022.101557
7. Toher C, Oses C, Esters M, Hicks D, Kotsonis GN, Rost CM, et al. High-entropy ceramics: Propelling applications through disorder. MRS Bulletin. 2022, 47(2):194–202. https://doi.org/10.1557/s43577-022-00281-x
8. Dippo OF, Vecchio KS. A universal configurational entropy metric for high-entropy materials. Scr Mater. 2021, 201:113974. https://doi.org/10.1016/j.scriptamat.2021.113974
9. Brahlek M, Gazda M, Keppens V, Mazza AR, McCormack SJ, Mielewczyk-Gryn A, et al. What is in a name: defining "high entropy" oxides. APL Mater. 2022, 10(11):110902. https://doi.org/10.1063/5.0122727
10. Miracle DB, Senkov ON. A critical review of high entropy alloys and related concepts. Acta Mater. 2017, 122(1):448–511. https://doi.org/10.1016/j.actamat.2016.08.081
11. Jiang S, Hu T, Gild J, Zhou N, Nie J, Qin M, et al. A new class of high-entropy perovskite oxides. Scr Mater. 2018, 142:116–20. https://doi.org/10.1016/j.scriptamat.2017.08.040
12. Gild J, Samiee M, Braun JL, Harrington T, Vega H, Hopkins PE, et al. High-entropy fluorite oxides. J Eur Ceram Soc. 2018, 38(10):3578–84. https://doi.org/10.1016/j.jeurceramsoc.2018.04.010
13. Djenadic R, Sarkar A, Clemens O, Loho C, Botros M, Chakravadhanula VSK, et al. Multicomponent equiatomic rare earth oxides. Mater Res Lett. 2017, 5(2):102–9. https://doi.org/10.1080/21663831.2016.1220433
14. Teng Z, Zhu LN, Tan YQ, Zeng SF, Xia YH, Wang YG, et al. Synthesis and structures of high-entropy pyrochlore oxides. J Eur Ceram Soc. 2020, 40(4):1639–43. https://doi.org/10.1016/j.jeurceramsoc.2019.12.008
15. Zhu JT, Meng XY, Zhang P, Li ZL, Xu J, Reece MJ, et al. Dual-phase rare-earth-zirconate high-entropy ceramics with glass-like thermal conductivity. J Eur Ceram Soc. 2021, 41(4):2861–69. https://doi.org/10.1016/j.jeurceramsoc.2020.11.047
16. Yang HB, Lin GQ, Bu HP, Liu HJ, Yang LX, Wang WJ, et al. Single-phase forming ability of high-entropy ceramics from a size disorder perspective: a case study of $(La_{0.2}Eu_{0.2}Gd_{0.2}Y_{0.2}Yb_{0.2})_2Zr_2O_7$. Ceram Int. 2022, 48(5):6956–65. https://doi.org/10.1016/j.ceramint.2021.11.252
17. Ridley M, Gaskins J, Hopkins P, Opila E. Tailoring thermal properties of multi-component rare earth monosilicates. Acta Mater. 2020, 195:698–707. https://doi.org/10.1016/j.actamat.2020.06.012
18. Ushakov SV, Hayun S, Gong WP, Navrotsky A. Thermal analysis of high entropy rare earth oxides. Materials. 2020, 13(14):3141. https://doi.org/10.3390/ma13143141
19. Poerschke DL, Krogstad JA. Rare earth oxide applications in ceramic coatings for turbine engines. In: Murty YV, Alvin MA, Lifton JP, editors. Rare Earth Metals and Minerals Industry: Status and Prospects. Springer; 2023.
20. Zhao ZF, Xiang HM, Chen H, Dai FZ, Wang XH, Peng ZJ, et al. High-entropy $(Nd_{0.2}Sm_{0.2}Eu_{0.2}Y_{0.2}Yb_{0.2})_4Al_2O_9$ with good high temperature stability, low thermal conductivity, and anisotropic thermal expansivity. J Adv Ceram. 2020, 9(5):595–605. https://doi.org/10.1007/s40145-020-0399-0
21. Zhaoa ZF, Chen H, Xiang HM, Dai FZ, Wang XH, Xu W, et al. High-entropy $(Y_{0.2}Nd_{0.2}Sm_{0.2}Eu_{0.2}Er_{0.2})AlO_3$: a promising thermal/environmental barrier material for oxide/oxide composites. J Mater Sci Technol. 2020, 47:45–51. https://doi.org/10.1016/j.jmst.2020.02.011
22. Corey ZJ, Lu P, Zhang GR, Sharma Y, Rutherford BX, Dhole S, et al. Structural and optical properties of high entropy $(La,Lu,Y,Gd,Ce)AlO_3$ perovskite thin films. Adv Sci. 2022, 9(29):2202671. https://doi.org/10.1002/advs.202202671
23. Tu T-Z, Liu J-X, Wu Y, Zhou L, Liang Y, Zhang G-J. Synergistic effects of high-entropy engineering and particulate toughening on the properties of rare-earth aluminate-based ceramic composites. J Adv Ceram. 2023, 12(4):861–72. https://doi.org/10.26599/JAC.2023.9220726
24. Pianassola M, Chakoumakos BC, Melcher CL, Zhuravleva M. Crystal growth and phase formation of high-entropy rare-earth aluminum perovskites. Cryst Growth Des. 2022, 23(1):480–88. https://doi.org/10.1021/acs.cgd.2c01130
25. Liao W, Tan Y, Teng Z, Jia P, Zhang H. High entropy $(Y_{1/5}Ho_{1/5}Er_{1/5}Yb_{1/5}Lu_{1/5})_3Al_5O_{12}$ with low thermal conductivity and high thermal stability. J Alloys Compd. 2023, 949:169736. https://doi.org/10.1016/j.jallcom.2023.169736
26. Wang KL, Zhu JP, Wang HL, Yang KJ, Zhu YM, Qing YB, et al. Air plasma-sprayed high-entropy $(Y_{0.2}Yb_{0.2}Lu_{0.2}Eu_{0.2}Er_{0.2})_3Al_5O_{12}$ coating with high thermal protection performance. J Adv Ceram. 2022, 11(10):1571–82. https://doi.org/10.1007/s40145-022-0630-2
27. Chen H, Zhao ZF, Xiang HM, Dai FZ, Xu W, Sun K, et al. High entropy $(Y_{0.2}Yb_{0.2}Lu_{0.2}Eu_{0.2}Er_{0.2})_3Al_5O_{12}$: a novel high temperature stable thermal barrier material. J Mater Sci Technol. 2020, 48:57–62. https://doi.org/10.1016/j.jmst.2020.01.056
28. Zhou C, Luo ZP, Du TF, Sun HF, Wang JM, Sun LC, et al. Directionally solidified high-entropy $(Y_{0.2}Gd_{0.2}Ho_{0.2}Er_{0.2}Yb_{0.2})_3Al_5O_{12}/Al_2O_3$ eutectic with outstanding crystallographic texture formation capability. Scr Mater. 2022, 220:114939. https://doi.org/10.1016/j.scriptamat.2022.114939
29. Zhong YJ, Xiang WS, He LT, Li JZ, Hao J, Tian ZL, et al. Directionally solidified $Al_2O_3/(Y_{0.2}Er_{0.2}Yb_{0.2}Ho_{0.2}Lu_{0.2})_3Al_5O_{12}$ eutectic high-entropy oxide ceramics with well-oriented structure, high hardness, and low thermal conductivity. J Eur Ceram Soc. 2021, 41(14):7119–29. https://doi.org/10.1016/j.jeurceramsoc.2021.07.049
30. Li ZQ, Zheng JF, Zhang WJ, Zheng Y, Zhao WJ, Xue LY, et al. A promising high-entropy thermal barrier material with the formula $(Y_{0.2}Dy_{0.2}Ho_{0.2}Er_{0.2}Yb_{0.2})_3Al_5O_{12}$. Materials. 2022, 15(22):8079. https://doi.org/10.3390/ma15228079
31. Pianassola M, Loveday M, Chakoumakos BC, Koschan M, Melcher CL, Zhuravleva M. Crystal growth and elemental homogeneity of the multicomponent rare-earth garnet $(Lu_{1/6}Y_{1/6}Ho_{1/6}Dy_{1/6}Tb_{1/6}Gd_{1/6})_3Al_5O_{12}$. Cryst Growth Des. 2020, 20(10):6769–76. https://doi.org/10.1021/acs.cgd.0c00887

32. Shannon RD. Revised effective ionic-radii and systematic studies of interatomic distances in halides and chalcogenides. Acta Crystallogr A. 1976, 32:751–67. https://doi.org/10.1107/S0567739476001551
33. Shannon RD, Prewitt CT. Effective ionic radii in oxides and fluorides. Acta Crystall B. 1969, B 25:925–46. https://doi.org/10.1107/S0567740869003220
34. Yamane H, Ogawara K, Omori M, Hirai T. Phase-transition of rare-earth aluminates ($RE_4Al_2O_9$) and rare-earth gallates ($RE_4Ga_2O_9$). J Am Ceram Soc. 1995, 78(9):2385–90. https://doi.org/10.1111/J.1151-2916.1995.Tb08673.X
35. Yamane H, Ogawara K, Omori M, Hirai T. Thermal-expansion and athermal phase-transition of $Y_4Al_2O_9$ ceramics. J Am Ceram Soc. 1995, 78(5):1230–32. https://doi.org/10.1111/j.1151-2916.1995.tb08474.x
36. Cruciani G, Matteucci F, Dondi M, Baldi G, Barzanti A. Structural variations of Cr-doped (Y,REE)AlO_3 perovskites. Z Kristallogr. 2005, 220(11):930–37. https://doi.org/10.1524/zkri.2005.220.11_2005.930
37. Kanke Y, Navrotsky A. A calorimetric study of the lanthanide aluminum oxides and the lanthanide gallium oxides: stability of the perovskites and the garnets. J Solid State Chem. 1998, 141(2):424-36. https://doi.org/10.1006/jssc.1998.7969
38. Yu Y-C, Godbole E, Berrios J, Hewage N, Poerschke DL. Slow sintering in garnet-containing Y and Gd zirconate-aluminate mixtures for thermal barrier coatings. J Am Ceram Soc. 2023, 106(8):4519–25. https://doi.org/10.1111/jace.19121
39. Godbole E, von der Handt A, Poerschke D. Apatite and garnet stability in the Al-Ca-Mg-Si-(Gd/Y/Yb)-O systems and implications for T/EBC: CMAS reactions. J Am Ceram Soc. 2022, 105(2):1596–609. https://doi.org/10.1111/jace.18179
40. Gandhi AS, Levi CG. Phase selection in precursor-derived yttrium aluminum garnet and related Al_2O_3-Y_2O_3 compositions. J Mater Res. 2005, 20(4):1017–25. https://doi.org/10.1557/Jmr.2005.0133
41. Iyi N, Inoue Z, Kimura S. The crystal structure of neodymium hexaaluminate. J Solid State Chem. 1984, 54(1):123–25. https://doi.org/10.1016/0022-4596(84)90139-7
42. Gadow R, Lischka M. Lanthanum hexaaluminate—novel thermal barrier coatings for gas turbine applications—materials and process development. Surf Coat Technol. 2002, 151:392–99. https://doi.org/10.1016/S0257-8972(01)01642-5
43. Wu P, Pelton AD. Coupled thermodynamic-phase diagram assessment of the rare earth oxide-aluminium oxide binary systems. J Alloys Compd. 1992, 179(1):259–87. https://doi.org/10.1016/0925-8388(92)90227-Z
44. Schmitt MP, Stokes JL, Rai AK, Schwartz AJ, Wolfe DE. Durable aluminate toughened zirconate composite thermal barrier coating (TBC) materials for high temperature operation. J Am Ceram Soc. 2019, 102(8):4781–93. https://doi.org/10.1111/jace.16317
45. Yu Y-C, Poerschke DL. Design of thermal and environmental barrier coatings for Nb-based alloys for high-temperature operation. Surf Coat Technol. 2022, 431:128007. https://doi.org/10.1016/j.surfcoat.2021.128007
46. Godbole EP, Hewage N, von der Handt A, Poerschke DL. Quantifying the efficiency of reactions between silicate melts and rare earth aluminate-zirconate T/EBC materials. J Eur Ceram Soc. 2023, 43(13):5626–35. https://doi.org/10.1016/j.jeurceramsoc.2023.05.009
47. Godbole E, Hewage N, Poerschke DL. Spreading and reaction behavior of CMAS-type silicate melts with multiphase Y and Gd aluminate-zirconate T/EBC materials. J Eur Ceram Soc. 2023, 43(14):6416-26 . https://doi.org/10.1016/j.jeurceramsoc.2023.05.046
48. Fabrichnaya O, Seifert HJ. Thermodynamic assessment of the ZrO_2-Yb_2O_3-Al_2O_3 system. Calphad. 2010, 34(2):206–14. https://doi.org/10.1016/j.calphad.2010.03.001
49. Lakiza SM, Lopato LM. Phase diagram of the Al_2O_3-ZrO_2-Nd_2O_3 system. J Eur Ceram Soc. 2006, 26(16):3725–32. https://doi.org/10.1016/j.jeurceramsoc.2005.12.005
50. Lakiza SM, Lopato LM. Phase diagram of the Al_2O_3-ZrO_2-La_2O_3 system. J Eur Ceram Soc. 2005, 25(8):1373–80. https://doi.org/10.1016/J.Jeurceramsoc.2005.01.014

How to cite this article: Yu Y-C, Nachlas WO, Poerschke DL. Phase stability and cation partitioning in compositionally complex rare earth aluminates and aluminate-zirconate mixtures. J Am Ceram Soc. 2024;107:1760–1775. https://doi.org/10.1111/jace.19375